Radiative electron capture studied in relativistic heavy-ion–atom collisions

Th. Stöhlker,* C. Kozhuharov, P. H. Mokler, A. Warczak,† F. Bosch, H. Geissel, R. Moshammer, and C. Scheidenberger
Gesellschaft für Schwerionenforschung, 64220 Darmstadt, Germany

J. Eichler‡
Bereich Theoretische Physik, Hahn-Meitner-Institut, 14109 Berlin, Germany and Fachbereich Physik, Freie Universität Berlin, 14195 Berlin, Germany

A. Ichihara and T. Shirai
Japan Atomic Energy Research Institute, Tokai-mura, Ibaraki 319-11, Japan

Z. Stachura
Instytut Fizyki Jądrowej, 31-342 Kraków, Poland

P. Rymuza
Instytut Badań Jądrowych, 05-400 Świerk, Poland
(Received 19 July 1994)

The process of radiative electron capture (REC) in relativistic collisions of high-Z ions with low-Z gaseous and solid targets is studied experimentally and theoretically. The observed x-ray spectra are analyzed with respect to photon angular distributions as well as to total K-REC cross sections. The experimental results for angle-differential cross sections are well reproduced by exact relativistic calculations which yield significant deviations from standard $\sin^2\theta$ distributions. Total cross sections for K-REC are shown to follow a simple scaling rule obtained from exact relativistic calculations as well as from a nonrelativistic dipole approximation. The agreement between these different theoretical approaches must be regarded as fortuitous, but it lends support to the use of the nonrelativistic approach for practical purposes.

PACS number(s): 34.70.+e

I. INTRODUCTION

In encounters of multiply charged ions and solid or gaseous matter a target electron may undergo a direct transition into a bound state of the projectile. In order to satisfy energy and momentum conservation laws such a process requires the presence of an additional particle. In the case of the nonradiative (Coulomb) electron capture, the third particle involved in the collision is the target atom. Alternatively, the coupling between the electron and the electromagnetic field of the moving ion may result in electron capture via simultaneous emission of a photon carrying away the energy and the momentum difference between the initial and final electron states. Radiative electron capture (REC) is the dominant electron-capture channel in fast encounters of heavy ions with light target atoms. If the kinetic energy of the electron in the projectile system greatly exceeds the initial binding energy in the target atom, one may disregard the latter, so that REC is equivalent to radiative recombination (RR) for highly stripped projectiles with free electrons. In a next improvement, one may take into account the electron binding by adopting the impulse approximation, which folds the initial electronic momentum distribution into the cross section for radiative recombination.

Within the impulse approximation, REC can be considered the same as time-reversed photoionization, a process that was already the subject of theoretical studies since the early days of the development of quantum mechanics [1,2]. The principle of detailed balance then allows one to derive cross sections for REC directly from those of photoionization. On this basis, Stobbe presented a general formalism for describing radiative recombination into arbitrary projectile states in the framework of a nonrelativistic dipole approximation [2]. This approach has been successfully and widely applied for understanding several astrophysical and related phenomena [3,4] as well as for predicting radiative recombination processes of exotic particles with bare ions [5–7]. More recently, a rigorous relativistic formalism was developed, which provides an accurate description of the REC and RR processes, even for the heaviest ions at relativistic velocities [8].

Although the process has been known for a long time, the emission of a REC photon was observed for the first

*Electronic address: t.stoehlker@gsi.de
†Permanent address: Uniwersytet Jagielloński, 30-059 Kraków, Poland.
‡Electronic address: Eichler@VAX.HMI.D400.DE

time in the early 1970's [9–11], and was a subject of extensive study during the last years [12–28]. Most of these experimental and theoretical efforts were stimulated by increasing interest in recombination processes due to their relevance to accelerator-storage-ring-based research [29–31] and for new developments in the field of electron-beam-ion sources [32]. For example, a detailed knowledge of this process is required for QED experiments using heavy bare and H-like projectiles [26,33–36], for predictions of charge-state distributions of relativistic heavy-ion beams [37,38] and in electron-beam ion traps [39], and for the estimation of beam losses in storage rings [40]. Very recently, its impact on nuclear physics experiments was also pointed out [41,45].

In this paper, we report on results of x-ray and charge-exchange experiments related to radiative capture. Owing to its relevance for the high-velocity regime, where experimental data are rather scarce, the main goal of the present investigation was to extend the information on REC up to the heaviest ion species (Au, Pb, Bi, U) at relativistic energies. The experimental as well as theoretical proofs of a scaling for K-REC cross sections, independently of the collision system, and its extension to total charge-exchange cross sections related to REC was one of the main subjects of these studies. The experiments were performed at two experimental areas of the Heavy-Ion Synchrotron and Storage-Ring facility (SIS and ESR) at the Gesellschaft für Schwerionenforschung (GSI) in Darmstadt [42] which are well suited for atomic-reaction studies: the fragment separator (FRS) [43] and the gas-jet target at the ESR [44].

Details of the experimental arrangements as well as the detection techniques and the data acquisition are described in Sec. II, where a typical raw charge-exchange particle spectrum and an x-ray emission spectrum are shown. Then, in Sec. III, the theory of radiative electron capture is discussed. In this section a rigorous relativistic treatment of REC is given, and the results are compared with the standard nonrelativistic dipole approximation. In Sec. IV, the shell differential radiative capture—essentially into the K shell—is discussed. Our experimental data for strong projectile potentials are also compared with all available literature data in the light of a general cross-section scaling. This scaling law for K-REC is extended in Sec. V to total radiative capture cross sections related to REC, which were determined via charge-exchange measurements. In Sec. VI the general agreement between theory and experiment is emphasized, and remaining open questions are discussed.

II. EXPERIMENTS DESCRIPTION

A. Experimental arrangements

The data presented were gained for different target-projectile combinations during various experiments utilizing the FRS for measurements with solid targets, and the internal gas jet of the ESR for measurements with gaseous targets. In Table I the relevant parameters for the collision systems studied are summarized, and the corresponding experiment location at the SIS and ESR facility is indicated. In addition, the resulting K-REC cross sections as well as the total charge-exchange cross sections related to radiative capture are given in the table.

For the experiments, the high-Z ion beams were preaccelerated at the linear accelerator (UNILAC) up to an energy of 11.4 MeV/u. Here, the ions traversed a first stripper foil and were directed into the SIS Synchrotron. After reaching the final beam energies (in the range between 90 and 1000 MeV/u) the ions were extracted from the SIS and injected into the transfer line toward the FRS or the ESR.

In the case of the experiments performed at the ESR, the ions were stripped in front of the storage ring to high charge states in a 100-mg/cm^2-thick Cu foil. The outgoing bare or H-like ion species were magnetically separated and finally injected into the ESR. Here the ions were cooled and accumulated up to a typical number of stored projectiles of about 10^7. After the stacking procedure, the gas jet was switched on. Molecular nitrogen with a thickness of 4×10^{11} particles/cm^2 was used as reaction target for all applied projectile species and collision energies. Additionally, for the uranium experiment, an Ar jet with a target thickness of 5×10^{11} particles/cm^2 could be used for reaction studies. During the experiment, the electron cooling was continously active, balancing the small beam energy losses in the gas target. A sketch of the experimental setup at the ESR gas-target is given in Fig. 1. As shown in the figure, the reaction area of the gas target was surrounded by three Ge(i) x-ray detectors mounted at observation angles of 48°, 90°, and 132° with respect to the beam axis. In contrast to the backward direction (132°), where a conventional x-ray detector with an active area of 500 mm^2 and a thickness of 10 mm was installed, the large Doppler broadening at 90° and 48° observation angles required the application of specially designed granular x-ray detectors. In particular, the x-ray detector mounted at the 48° position (crystal thickness 12 mm) was subdivided into seven independent segments (parallel stripes with active areas of 3.5×24mm^2 each, furnished with separate readouts). This detector delivered seven independent spectra with relatively small individual Doppler broadenings. The Doppler shift was corrected separately for each segment. The resulting sum spectrum combines the advantage of the large total solid angle of $\Delta\Omega/4\pi=3\times10^{-3}$ with a narrow Doppler broadening of one segment. The segmented 5-mm-thick Ge(i) detector at 90° observation angle covered in total a solid angle of $\Delta\Omega/4\pi=3\times10^{-4}$. The detector was divided into five independent segments, four quadrants (forward, backward, top, and bottom) with the same size of 65 mm^2 each, and one central part with an active area of 36 mm^2. The detectors at the forward and backward angles were separated by 100-μm-thick Be windows from the high-vacuum system of the ESR, whereas for 90° a 50-μm-thick stainless-steel window was used. Downstream from the target area, behind the next dipole magnet, a position-sensitive multiwire detector (MWPC) detected ions having captured one electron in collisions with the target atoms (molecules). For the absolute normalization of the data, the current of the circulating ion beam was measured by a calibrated current transformer

installed in the ring, whereas the revolution frequency of the particles was determined via the analysis of the Shottky-noise spectrum.

In Fig. 2, the relevant features of the experimental arrangement at the FRS are shown. For the charge-exchange experiments at the FRS, a high-resolution ion-optical spectrometer [43], the slow extraction mode of the SIS was utilized, with a typical spill length of 2 s and a repetition rate of one spill per 6 s. At the entrance of the FRS the ions passed through an Al or Cu stripper foil (depending on the experimental requirements). Thereafter, the emerging charge states were magnetically separated. Using collimator slits mounted at the first dispersive focal plane, ion beams with one well-defined charge state were produced, and focused after a further magnetic purification onto thin charge-exchange foils. The thickness of the self-supporting beryllium, carbon, or aluminum reaction targets, with diameters between 2 and 3 cm, was typically 500 $\mu g/cm^2$. This guaranteed a single collision condition for all projectile species and energies used. The diameter of the beam spot on the target was typically between 3 and 5 mm. Downstream from this reaction foil the outgoing charge states were once again magnetically analyzed and separated. A 100% transmission efficiency was permitted by ion-optical settings of the separator which were especially developed for these atomic physics experiments [43]. In charge-exchange experiments the ions were detected by a position-sensitive MWPC counter installed at the end of the beam line, whereby the beam intensity on the detector was reduced to about 10^3 ions/s.

In the case of a dedicated x-ray–particle coincidence experiment, the reaction area was viewed by two, opposite facing granular Ge(i) detectors (for the crystal segment geometry compare the 90° detector used for the ESR experiments as discussed above). One of the detectors was mounted close to the target foils with a total solid angle of $\Delta\Omega/4\pi = 3\times10^{-3}$. The second one was placed farther apart to reduce Doppler broadening, allowing us to resolve the $K\alpha_1$ and $K\alpha_2$ transitions produced via electron capture to the projectile. Both the detectors were separated from the FRS vacuum by 50-μm-thick stainless-steel windows. For this kind of experiment, the MWPC counter for the particle detection was replaced by three plastic scintillator detectors, permitting a high particle detection rate of up to 10^7 ions/s. They also enabled us to register independently ions with charge state $Q-1$ (capture into the projectile), Q (incident charge state), and $Q+1$ (projectile electron loss).

B. Data acquisition and analysis

Standard NIM and CAMAC modules were used in all experiments for data acquisition. The x-ray spectra sup-

TABLE I. Measured K-REC and total capture cross sections related to REC for studied projectile-target combinations. The relevant parameters for the collision systems are given together with the experiment location at the SIS/ESR facility. The uncertainties quoted for the measured cross-section values comprise both systematic as well as statistical errors.

Ion	Z	Q	Energy (MeV/u)	Targets used	Experiment location	$\sigma^{K\text{-REC}}$ (barn)	σ^{total} (barn)
Au	79	78+	221	C	FRS [46,47]		326±65
			224	N_2	ESR [60]		728±146
			230	N_2	ESR [62]		602±120
Au	79	79+	288	N_2	ESR [62]		770±154
			587	Al	FRS [46]		255±51
			989	C	FRS [46]		42±8
			989	Al	FRS [46]		81±16
Pb	82	81+	219	N_2	ESR [63]	263±79	728±218
			277	N_2	ESR [63]		308±123
Pb	82	82+	277	N_2	ESR [63]	535±161	1113±223
Bi	83	82+	82	C	FRS [64]	680±136	
			116	C	FRS [64]	371±74	
			169	C	FRS [64]	239±48	
Bi	83	83+	169	C	FRS [64]		1111±222
U	92	91+	295	N_2	ESR [36]	290±87	706±141
			295	Ar	ESR [36]	588±176	
U	92	92+	295	Be	FRS [36]		323±65
			295	C	FRS [36]		503±50
			295	N_2	ESR [36]	569±171	1084±217
			295	Ar	ESR [36]	1069±321	

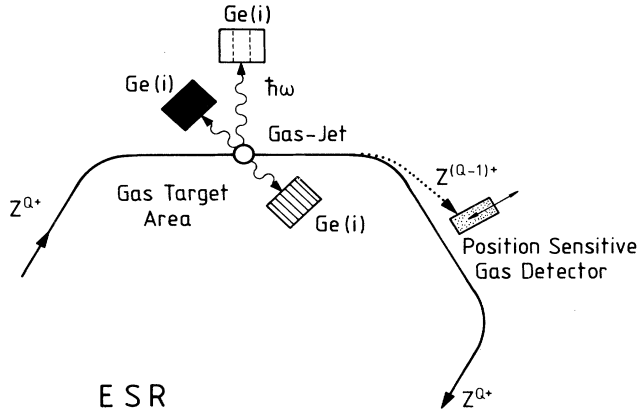

FIG. 1. Experimental setup to measure electron capture at the storage ring ESR: Interaction region with the gas-jet is viewed by Ge(i) x-ray detectors. The x-ray emission is measured in coincidence with down-charged projectiles detected behind the next dipole magnet (not indicated in the figure).

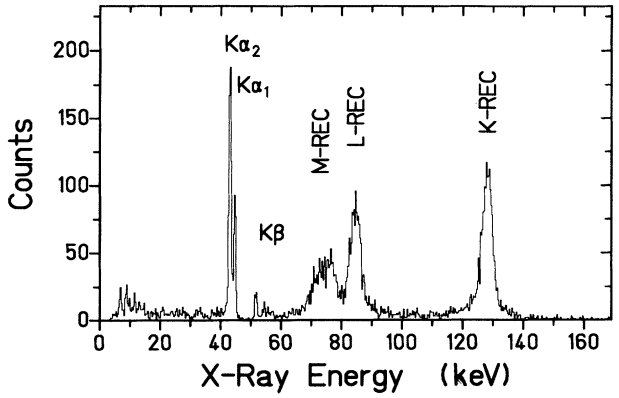

FIG. 3. X-ray spectrum for 230-MeV/u $Pb^{81+} \rightarrow N_2$ collisions associated with projectiles which captured one electron. The spectrum was taken at the ESR storage ring at an observation angle of $\theta = 132°$. Note that the spectrum is not corrected for detection efficiency. X-ray energies are given in the laboratory frame.

plied by each detector (and detector segment) were recorded independently event by event in coincidence with each particle counter. All x-ray and particle detectors were connected to fast CAMAC scalers in order to correct for possible electronic dead time effects. However, the latter was avoided by keeping the event rate below 100 Hz, corresponding to primary beam intensities below 10^6 particles per second. All x-ray detectors, including their electronics, were energy and efficiency calibrated with ^{182}Ta, ^{133}Ba, and ^{241}Am sources. The systematic error introduced by the efficiency calibration was largest for x-ray energies higher than 130 keV, and can be estimated to be of the order of 10%. For the registered coincident x-ray events, the random coincidences were found to be almost negligible. Nevertheless, for data evaluation, the random contributions were subtracted from the true coincident x-ray spectra in all cases. The solid angles of the x-ray detectors could be precisely deduced by laser-assisted trigonometry.

In Fig. 3, a typical x-ray spectrum is shown, measured by the backward detector ($\theta = 132°$) at the internal gas target of the ESR. The redshifted spectrum was taken in coincidence with the down-charged ions for 230-MeV/u $Pb^{81+} \rightarrow N_2$ collisions (not corrected for photon detection efficiency). The x-ray energy range covers the $L\alpha$, β and $K\alpha,\beta$ transition energies as well as the energy regime for REC into bound projectile states. As seen in the figure, the spectrum is entirely governed by REC into the ground and excited states of the projectile. Due to the partially blocked K shell of the projectiles, the yield of K- and L-REC photons is comparable. REC into excited states leads partially, via cascades, to the well-resolved $K\alpha_1$ and $K\alpha_2$ transitions. For completeness we would like to add that the x-ray detectors located at 48° and 90° were essentially used for the spectroscopic analysis of the characteristic Ly-α and $K\alpha$ transitions [36]. In particular, the REC transitions could not be measured by these detectors with sufficient statistics, as a consequence of the low detection efficiency due to the strong blueshift at forward direction ($\theta = 48°$) and to the very small solid angle at $\theta = 90°$.

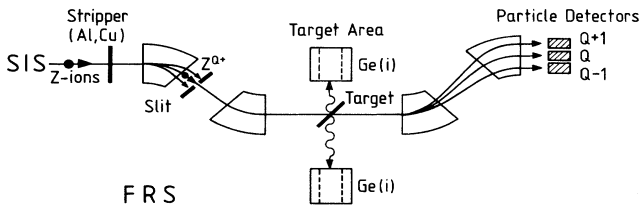

FIG. 2. Experimental setup for charge-exchange measurements at the FRS: Heavy ions with an atomic number Z and with a selected initial charge state Q are focused on the reaction target (Be, C, or Al foils). Projectile x rays are registered by two segmented Ge(i) detectors. The emerging charge states are analyzed by the two following dipole stages. In order to keep this schematic view transparent the ion trajectories are presented in an oversimplified manner.

The absolute charge-exchange cross sections in solid targets, measured at the FRS, were determined either directly from the scaler increments of the scintillator detectors or from the position spectra recorded by a MWPC counter. Figure 4 shows, as an example, the charge-state spectrum measured at the FRS for 221-MeV/u Au^{78+} ions which have traversed a 400-μg/cm^2-thick C target.

The systematic uncertainties of the measured total cross sections, extracted out of the scaler increments of the scintillator detectors, can be attributed to possible amplitude variation of the fast timing signals depending on the primary beam intensity used. This was checked online by comparing the ratios of the scaler increments for different primary beam intensities, which were varied between 10^4 and 10^6 particles per second. Within an accuracy of better than 10% we observed no such fluctuations. In the case where MWPC counters were used, the main uncertainty arises from a possible position-

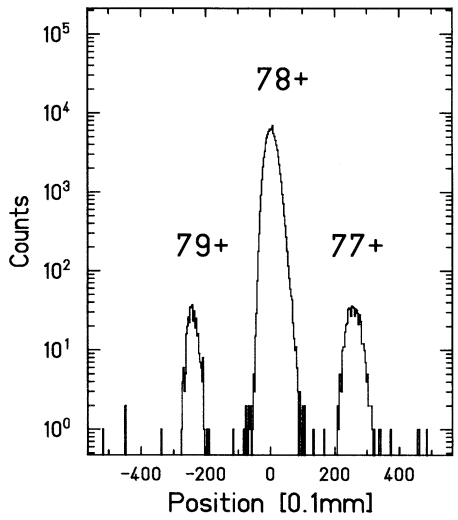

FIG. 4. Measured charge-state spectrum of incident H-like Au^{78+} ions at 230 MeV/u after penetrating through a 400-$\mu g/cm^2$ thin C target.

dependent detection efficiency. By changing the positions of the various charge states on the MWPC counters, no position-dependent detection efficiency could be observed within a statistical uncertainty of about 10%. Within the statistical uncertainties, the results of both methods (MWPC and plastic counters) were found to be consistent.

In contrast to the FRS experiments, where the thicknesses of the solid targets are known within a precision of about 5%, the effective target thickness of the internal gas target gives the largest uncertainty contribution for the ESR data. Here an overall uncertainty of 20% must be assumed.

III. THEORY

In radiative electron capture (REC) during a collision between a high-Z projectile and a low-Z target, where Z is the atomic charge number, the loosely bound target electrons can be regarded as quasifree. It is then a good approximation to substitute for REC the radiative recombination (RR) of the projectile with free electrons moving with the velocity v toward it. This process is the inverse of the photoelectric effect, in which a photon with energy $\hbar\omega$ (and wave number $\mathbf{k}$) hits the projectile atom and ejects an electron with the velocity v [12].

A. Nonrelativistic dipole approximation

For a first estimate, we assume that $\hbar\omega \ll m_e c^2$ and $\alpha Z \ll 1$, where m_e is the electron mass, c the speed of light, $\alpha = 1/137.036$ the fine-structure constant, and Z now the projectile charge number. Under these conditions, it is justified to adopt the nonrelativistic dipole approximation for calculating the cross section for the photoelectric effect or for radiative recombination. Within this framework, the general result for radiative recombination into an arbitrary final (n,l) state of a bare ion has been given by Stobbe [2] in the form

$$\sigma_{nl}^{\text{Stobbe}} = \frac{\pi^2}{3}\alpha^3 a_0^2 \left[\frac{\nu^3}{1+\nu^2}\right]^2 \times\{(l+1)[C_{nl}^{l+1}(\nu)]^2 + l[C_{nl}^{l-1}]^2\}\ , \tag{1}$$

where $\nu = \alpha Z/n\beta$ is the Sommerfeld parameter, $\beta = v/c$, and a_0 the Bohr radius. The quantities $C_{nl}^{l\pm1}$ are the dipole matrix elements for transitions between bound states (n,l) and continuum states with angular momenta $l\pm1$ and energy E_{kin}. Expression (1) has been evaluated by various authors [2,7,48,49], and tabulated results can be found in [49]. An estimate for REC cross sections for very light target atoms ($\alpha Z_T \ll 1$) can be obtained from Eq. (1) by multiplying σ^{Stobbe} by the number Z_T of quasifree electrons in the target [12]. If only capture into the $1s$ state is considered, Eq. (1) simplifies to the well-known expression [50]

$$\sigma_{1s}^{\text{Stobbe}} = 9.165\times\left[\frac{\nu^3}{1+\nu^2}\right]^2 \frac{e^{-4\nu\arctan(1/\nu)}}{1-e^{-2\pi\nu}} 10^{-21}\text{cm}^2\ . \tag{2}$$

It is interesting to note that the projectile charge number Z and the velocity v enter the Stobbe cross sections (1) or (2) not separately, but only in the combination Z/v occurring in the Sommerfeld parameter ν. Within Stobbe's nonrelativistic dipole approximation, the differential cross section in the laboratory system is given by

$$\frac{d\sigma_{1s}^{\text{Stobbe}}}{d\Omega} = \sigma_{1s}^{\text{Stobbe}} \frac{3}{8\pi}\sin^2\theta\ , \tag{3}$$

where $\theta = \theta_{\text{lab}}$ denotes the angle between the directions of the incoming electron and the emitted photon in the laboratory system.

The Stobbe approximation is valid only for $v \ll c$ and for rather low photon energies. If the photon wavelength becomes comparable to the K-shell radius, it is not sufficient to confine oneself to the lowest-order term in the expansion of the photon plane wave; that is, one has to take into account the retardation. Furthermore, for a fast moving projectile, one has to Lorentz transform the angular distribution from the projectile system into the laboratory system. It has been shown by Spindler [16] that both effects tend to cancel each other in the angular distribution, so that a $\sin^2\theta$ distribution may still be valid at higher collision energies. Nevertheless, the Stobbe treatment becomes questionable for high-Z projectiles.

B. Exact relativistic treatment

If one adopts the picture of quasifree target electrons moving in the target with a momentum distribution $\rho(\mathbf{q})$, a rigorous description of REC proceeds in the following steps; see, e.g., [8,51]: (a) One calculates the exact relativistic differential cross section of the photoelectric effect for the projectile in the projectile system. (b) By the principle of detailed balance, the corresponding cross section for radiative recombination is derived. (c) Using the im-

pulse approximation, this cross section is convoluted with the momentum distributions of the electrons in the target atom. (d) The resulting cross section is Lorentz transformed to the laboratory system.

(a) Relativistic cross sections for photoionization have been calculated in the past [52,53] and are, usually for the K shell, available in tabulated form [52]. These existing tabulations for exactly evaluated cross sections are sometimes not suitable for calculating differential cross section on a sufficiently dense mesh. Therefore, an independent computer code has been developed [8], which assumes unpolarized photons and electrons and uses exact wave functions $\psi_{j_b,\mu_b}(\mathbf{r})$ and $\psi_{\mathrm{p},m_s}(\mathbf{r})$ for bound and continuum states, respectively. For a given photon energy, the differential cross section for a single electron is

$$\frac{d\sigma_{\mathrm{ph}}}{d\Omega}=\frac{\alpha^3 m_e c^2}{4\hbar\omega}\frac{a_0^2}{2j_b+1}\sum_{\mu_b}\sum_{m_s}|M_{\mathrm{p},b}(m_s,\lambda_+,\mu_b)|^2 , \quad (4)$$

where the average over the $(2j_b+1)$ angular momentum projections μ_b in the bound state b is taken, and a summation over the spin projections $m_s=\pm\frac{1}{2}$ of the emitted electron is performed. Furthermore, the average is taken over the circular polarizations $\lambda_+=1$ and $\lambda_-=-1$ of the incoming photon. Because of the summation over all other angular momentum projections, μ_b and m_s, this is equivalent to taking one photon polarization, e.g., $\lambda_+=1$ only. The transition matrix element is

$$M_{\mathrm{p},b}(m_s,\lambda_+,\mu_b)=\int\psi^{\dagger}_{\mathrm{p},m_s}(\mathbf{r})\alpha\cdot\hat{\mathbf{u}}_+e^{i\mathbf{k}\cdot\mathbf{r}}\psi_{j_b,\mu_b}(\mathbf{r})d^3r , \quad (5)$$

where α is the Dirac alpha matrix and $\hat{\mathbf{u}}_+$ is the unit vector of photon polarization. Within $\psi_{\mathrm{p},m_s}(\mathbf{r})$, the summation over the partial waves with the Dirac quantum number κ is carried to a maximum value $|\kappa_{\max}|$ as required for convergence. The integration is performed numerically.

(b) Once the cross section $\sigma_{\mathrm{ph}}(\omega',\theta')$ for photoionization in the projectile frame (denoted by primed quantities) has been computed, it is a simple matter to write down the cross section $\sigma_{\mathrm{RR}}(E',\theta')$ for radiative recombination. By the principle of detailed balance, the cross section for radiative recombination is written as

$$\frac{d^2\sigma_{\mathrm{RR}}(E',\theta')}{dE'd\Omega'_{\mathrm{ph}}}=(2j_b+1)\left[\frac{\hbar\omega'}{m_e c^2}\right]^2\frac{1}{\beta^2\gamma^2}\frac{d^2\sigma_{\mathrm{ph}}(E',\theta')}{dE'd\Omega'_{\mathrm{el}}} . \quad (6)$$

Here the factor $(2j_b+1)$ converts the averaging of Eq. (4) into a summation, while $\beta=v/c$, and $\gamma=(1-\beta^2)^{-1/2}$ is the Lorentz factor.

(c) From the exact cross section (6) for radiative recombination, one can derive the REC cross section by adopting the impulse approximation and convoluting σ_{RR} with the momentum distribution $\rho(\mathbf{q})$ of the electrons in the target atom. Denoting the initial total energy (including the rest mass) of the initial and final atomic states in the projectile frame by E'_i and E'_f, respectively, one obtains

$$\frac{d^2\sigma_{\mathrm{REC}}(\omega',\theta')}{d\omega'd\Omega'}=\int d^3q\frac{d\sigma_{\mathrm{RR}}(\mathbf{q}')}{d\Omega'}\rho(\mathbf{q})\delta(\hbar\omega'+E'_f-E'_i) , \quad (7)$$

where the δ function ensures energy conservation. If the transverse momentum distribution of the electrons in the initial state i is ignored, one may express the REC cross section with the aid of the Compton profile $J_i(q_z)$. Following Ichihara, Shirai, and Eichler [8], here we use a rigorous relativistic addition of momenta, which takes into account that the effective momentum of the target electron with respect to the projectile does not usually coincide with the beam direction. The momentum density $\rho(\mathbf{q})$ is obtained by Fourier transforming appropriate Roothaan-Hartree-Fock wave functions [8].

(d) Finally, one has to transform all quantities into the laboratory system (unprimed quantities) [51]:

$$\omega'=\gamma\omega(1-\beta\cos\theta) ,$$
$$\cos\theta'=\frac{\cos\theta-\beta}{1-\beta\cos\theta} . \quad (8)$$

If one is interested in the angular distribution at a fixed frequency, say, at the resonance frequency ω'_0 in the projectile system or in the complete integral over the resonance line, one obtains the laboratory angular distribution by multiplying with the well-known ratio

$$\frac{d\Omega'}{d\Omega}=\frac{1}{\gamma^2(1-\beta\cos\theta)^2} \quad (9)$$

of the differential solid angles, so that the desired single-differential cross section becomes

$$\frac{d\sigma_{\mathrm{REC}}(\theta)}{d\Omega}=\frac{d\sigma_{\mathrm{REC}}(\theta')}{d\Omega'}\frac{d\Omega'}{d\Omega} . \quad (10)$$

Figure 5 gives the single-differential K- and L-REC cross sections for 295-MeV/u $U^{92+}\rightarrow N$ collisions as a function of the observation angle in the laboratory system. In the case of the K-REC angular distribution, the result of the full relativistic calculation [see full line in Fig. 5(a)] is compared with the nonrelativistic angular distribution given by Eq. (3) [compare dashed-dotted line in Fig. 5(a)]. In addition, the experimental differential K- and L-REC cross sections are presented in the figure, measured at an observation angle of $\theta=132°$ in 295-MeV/u $U^{92+}\rightarrow N_2$ collisions. For comparison, we reduced all our data for the molecular gas target (N_2) to an atomic nitrogen target by assuming $\sigma(N)=\sigma(N_2)/2$. The data (see full points in Fig. 5) are discussed in Sec. IV. According to the relativistic description, the differential cross sections for K-REC show a pronounced deviation from symmetry around $\theta=90°$, and the maximum of the distribution is markedly shifted into the forward direction. As discussed in detail by Ichihara, Shirai, and Eichler [8], this behavior is essentially associated with the occurrence of magnetic (spin-flip) transitions which are not considered by a nonrelativistic theory.

C. Comparison of theoretical total RR cross sections

Even though the differential cross sections may differ markedly from the form (3) given by the nonrelativistic dipole approximation, it was noted by Stöhlker and co-

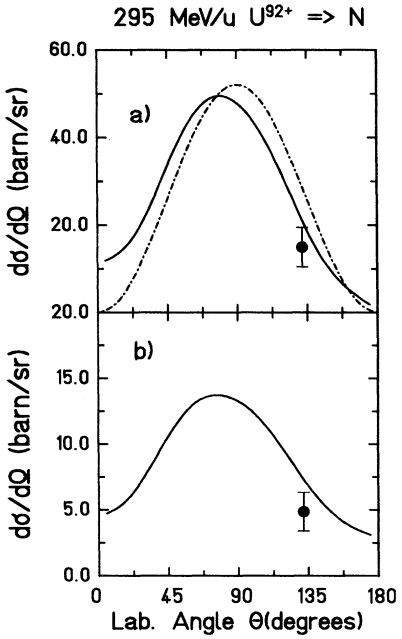

FIG. 5. Differential K-REC cross sections (a) and L-REC cross sections (b) are given by the full points for $U^{92+} \rightarrow N_2$ collisions at 295 MeV/u. For comparison with the theoretical predictions for $U^{92+} \rightarrow N$ collisions, the experimental cross sections were divided by a factor of 2. The solid lines in (a) and (b) give the corresponding relativistic angular-differential cross-section predictions [8]. The dashed-dotted line in (a) was calculated using the nonrelativistic dipole approximation [see Eq. (3)].

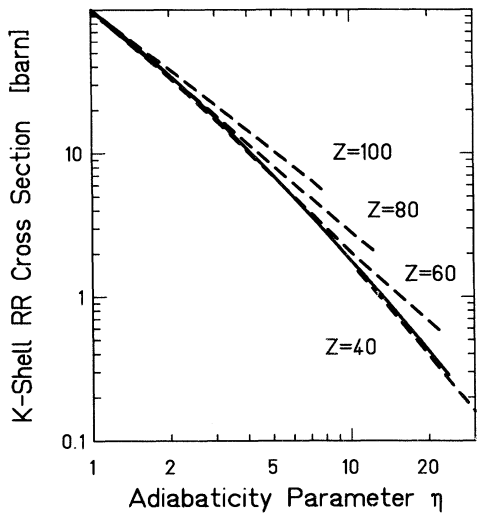

FIG. 6. Calculated relativistic radiative recombination cross sections [8] into the K shell of projectiles with atomic numbers of $Z=40$, 60, 80, and 100 (dashed lines) in comparison with the dipole approximation [2] (full line) as a function of the η parameter [compare Eq. (11)]. For $Z=40$ the relativistic calculations coincides completely over the full η range with the predictions of the dipole approximation.

workers [25,54] from a comparison with tabulated photoionization cross sections that this is not the case for total cross sections, a result that was recently confirmed by systematic relativistic calculations by Ichihara, Shirai, and Eichler [8]. In order to show this for a large number of collision systems, it is useful to define an adiabaticity parameter η by connecting it to the Sommerfeld parameter ν through the relation

$$\eta = 1/\nu^2 \simeq 40.31 \times \frac{E_{\rm kin}({\rm MeV/u})}{Z^2} \ . \qquad (11)$$

This parameter decides whether a collision is fast ($\eta > 1$) or slow ($\eta < 1$). The η parameter is convenient for presenting RR or REC cross sections per target electron independently of the collision system. It is important to note that for the η definition of Eq. (11) the relation $E_{\rm kin} = \frac{1}{2} M v^2$ was applied as if the projectile speed was nonrelativistic (M is the mass of the projectile).

Before comparing with experimental data, we first present theoretical results in Figs. 6–8, obtained, on the one hand, with the nonrelativistic dipole approximation Eqs. (1) and (2), and on the other hand from exact relativistic calculations using the computer code of [8]. While in Fig. 6, for $\eta > 1$, the nonrelativistic dipole approximation yields a single universal curve for $\sigma_{1s}^{\rm Stobbe}$ as a function of η, the exact relativistic treatment leads to separate curves for each of the projectile charges Z. It is interesting to note that the family of the exactly calculated curves (see dashed lines in the figure) do not deviate very much from the one of the nonrelativistic dipole approximation (full line in Fig. 6). This is true even for relativistic energies (up to 1 GeV/u), where the energy-velocity relation is far from the nonrelativistic limit assumed in definition (11), and where the dipole approximation certainly breaks down. In Fig. 7, the comparison between the full relativistic and nonrelativistic theories is extended to total RR cross sections. For the dipole approximation, all final n states up to $n=20$ were considered, whereby the prescription for evaluating Eq. (1) given by Burgess [48] was applied, which enables a fast analytical computation for any arbitrary (n,l) state. The dashed lines in Fig. 7 represent the total RR cross sections of the fully relativistic calculations for various projectile Z systems ($Z=40$, 60, 80, and 100). Here only capture to the K, L, and M shells is considered. Radiative capture into final projectile states with $n > 3$ can be neglected, since in the high-collision velocity regime, $\sigma^{\rm RR}$ scales approximately with $1/n^3$ [51]. This is illustrated in Fig. 8, where the cross sections for capture into the K, $K+L$, and $K+L+M$ shells of various bare projectile systems are plotted versus the projectile energy (for σ_K compare the dashed lines, for $\sigma_K+\sigma_L$ compare the dashed-dotted lines and for $\sigma_K+\sigma_L+\sigma_M$ compare the full lines in Fig. 8, respectively).

Comparing the calculated total RR cross sections plotted in Fig. 7 as a function of the η parameter, the same behavior as for K-REC can be stated, i.e., the theoretical data fall on one common curve for low-η values ($\eta \leq 1$), whereas for higher-η values the data diverge slightly. We have to add that for $Z=60$ the theoretical curve coincides completely, over the full η range, with the total capture cross sections derived from the dipole approximation, cf. Eq. (1). For $Z=60$ the curve includes collision energies up to 2 GeV/u.

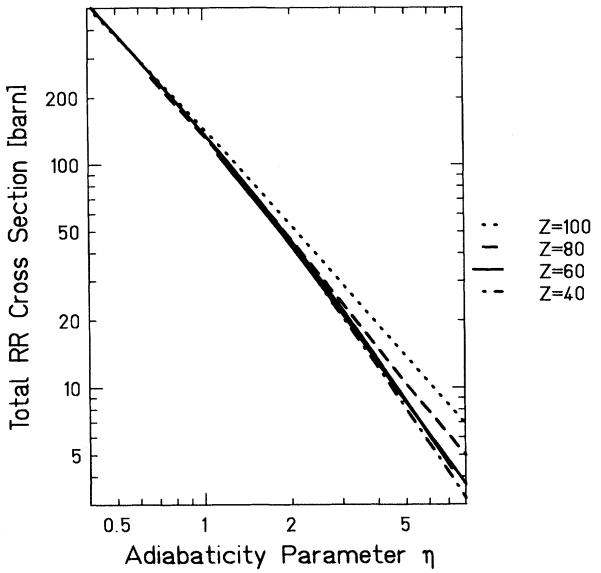

FIG. 7. Calculated total relativistic radiative recombination cross sections [8] for ions with an atomic number of $Z=40$ (dashed-dotted line), $Z=80$ (dashed line), and $Z=100$ (dashed-dotted line) in comparison with the dipole approximation [2] (full line) as a function of the η parameter [compare Eq. (11)]. For $Z=60$ the relativistic calculation coincides completely over the full η range with the predictions of the dipole approximation.

The astonishing agreement between relativistic calculations and the classical approach observed in Figs. 6 and 7, at least for atomic numbers that are not too high, must be regarded as fortuitous. Nevertheless, it provides a legitimation for the convenience of comparing experimental total cross sections with the easily calculated universal Stobbe curve. This is done in Sec. V.

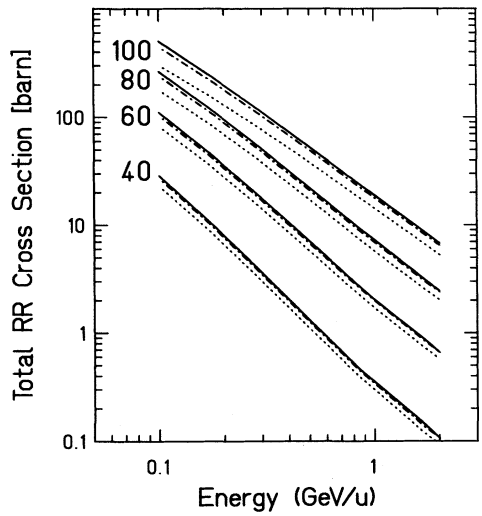

FIG. 8. Relativistic radiative recombination cross sections for capture into the K, $K+L$, and $K+L+M$ shells for various projectiles ($Z=40$, 60, 80, and 100) are plotted vs the projectile energy (for σ_K compare the dashed lines, for $\sigma_K+\sigma_L$ the dashed-dotted lines, and for $\sigma_K+\sigma_L+\sigma_M$ the full lines, respectively).

IV. X-RAY PRODUCTION RELATED TO REC

A. X-ray energy spectra

In Fig. 9, we present the efficiency corrected x-ray spectra, taken in coincidence with the down-charged ions at the internal gas target of the ESR. The first two spectra [Figs. 9(a) and 9(b)] correspond to capture from N_2 molecules into bare U^{92+} and H-like U^{91+} ions which were taken at a collision energy of 295 MeV/u. The third spectrum [Fig. 9(c)] was recorded for the collision system $U^{92+} \rightarrow Ar$ at the same collision energy. All coincidence spectra plotted in the figure were observed at a detection angle of 132°. The energy range displayed in the figure covers the x-ray energy regime relevant for radiative electron-capture transitions into the ground state and into excited states of the projectile. As seen in Fig. 9, all

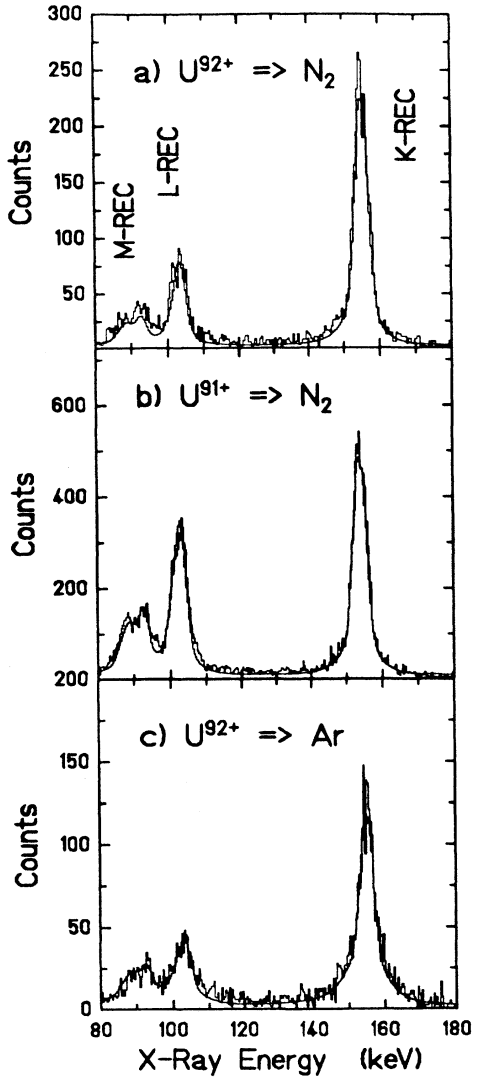

FIG. 9. X-ray spectra corrected for the energy-dependent detector efficiency for incident U^{91+} and U^{92+} ions on N_2 and Ar targets at 295 MeV/u. The spectra were accumulated at the ESR gas target in coincidence with the down-charged ions.

these REC contributions are clearly resolved. The comparison between Figs. 9(b) ($U^{91+} \rightarrow N_2$) and 9(a) ($U^{92+} \rightarrow N_2$) manifests a reduction by a factor of 2 of the K-REC intensity, in comparison to REC into excited projectile states, due to the partially blocked K-shell channel. Moreover, a comparison of the spectra plotted in Figs. 9(a) and 9(c) illustrates that the REC linewidth is correlated with the target atomic number Z and reflects the Compton profile of the initially bound target electrons. Due to the stronger binding of the K-shell electrons in Ar, the base of the REC lines is skewed and considerably broader than for the N_2 target.

The centroids of the lines ($\bar{E}_{\mathrm{REC}}$) appear close to the energy given by [8,55]

$$\bar{E}_{\mathrm{REC}} = \frac{E_{\mathrm{kin}} + |E_j| - \gamma |E_i|}{\gamma(1-\beta\cos\theta)} , \tag{12}$$

where E_j and E_i denote the final and initial electron binding energies of the active electron. By knowing precisely the kinetic energy (E_{kin}) of the ions as well as the observation angle θ, the relation between the binding energy of the final state E_j and the REC photon energy can be applied as an important tool for the spectroscopic study of binding energies of high-Z ions [26,55]. Here it is important to note that the electron momentum within the target also has a transverse component with respect to the beam direction. Therefore, as discussed by Ichihara, Shirai, and Eichler [8] (compare also Sec. III), the direction of the electron momentum seen by the projectile deviates slightly from the z direction defined by the beam. This complication has never been considered before in connection with the analysis of REC centroid energies [26,55]. We expect that the integration over the spherical momentum distribution of target electrons will lead essentially to an additional broadening, and also to a slight shift of the REC centroid energies. However, for a precise determination of the total binding energies E_j this effect must be taken into account. Here we do not extract the binding energies, as the uncertainties for both the x-ray energy efficiency corrections and the counting statistics are too large.

B. Radiative capture to the K shell

In order to obtain the differential K- and L-REC cross-section values, the following fit formula has been applied to the line-shape analysis of the measured REC spectral distributions:

$$\frac{d^2\sigma}{d\Omega' d\hbar\omega'} = \sum_j c_j \left[\frac{1}{\gamma\beta c} \sum_i \int dq_z \mathcal{J}_i(q_z) \frac{d\sigma_j}{d\Omega'} \delta_j \right] , \tag{13}$$

where the primed variables denote the projectile frame, and the unprimed quantities the target frame. Furthermore, $\mathcal{J}_i$ is the Compton profile of the electron in the initial target orbital i, while q_z is the projection of the electron momentum onto the beam axis, and the quantities c_j are fitting parameters. For the δ function, compare Eq. (7). Following the description of Kleber and Jakubassa [12], the quantity in the square brackets of Eq. (13) represents the double differential cross section for REC into a specific projectile substate j. For the differential cross section $d\sigma_j^{\mathrm{REC}}/d\Omega'$ we applied the prescription of the dipole approximation [2], which is known to predict correctly the energy dependence of REC. For the Compton profiles the calculated values of Biggs, Mendelsohn, and Mann [56] were used. The results were transformed to the laboratory frame and convoluted by a rectangular function in order to account for the Doppler broadening. Using a χ^2 minimizing routine, the resulting line shape was adjusted to the measured REC distribution via simultaneous variation of the parameters c_j. In addition, a linear background was subtracted. As depicted in Fig. 9 by the full curves, a good agreement between the applied spectral line analysis and the measured REC spectra can be stated.

In Fig. 5, the differential K- and L-REC cross-section values gained by the spectrum analysis are compared with exact relativistic calculations (see full points in Fig. 5). Within the total experimental uncertainty, a fair agreement in the absolute values between experiment and relativistic theory is found. Here the prediction of the dipole approximation [dashed-dotted line in Fig. 5(a)] overestimates considerably the experimental value of 132°. The extracted K- to L-REC intensity ratios at $\theta = 132°$ of 2.77 ± 0.12 (295 MeV/u, $U^{92+} \rightarrow N_2$) and of 2.92 ± 0.14 (295 MeV/u, $U^{92+} \rightarrow$ Ar) are in remarkable agreement with the theoretical value of 2.84. The experimental cross-section ratios are determined much more precisely than the absolute cross-section data, as they are only affected by the statistical uncertainty. The obtained results indicate strongly that the applied relativistic theory delivers a correct description of the REC process involving high-Z ions at relativistic collision energies. The discrepancy of the differential cross-sections between the relativistic exact calculations and the nonrelativistic approach [see the dotted line in Fig. 5(a)] at 132° amounts to about 20%. The latter approach has been commonly used for the evaluation of total cross sections for REC into the K shell. The application of this approach to the discussed collision systems would underestimate the derived total K-REC cross-section values. Therefore, in this work, the total cross sections were extracted from the measured differential values via normalization to the relativistic exact angular distributions. The angular distributions predicted by the fully relativistic theory [8] could already be verified experimentally for the case of L-REC into the j substates of He-like U^{90+} at a collision energy of 89 MeV/u [54].

In Fig. 10 the resulting total K-REC cross sections, normalized to the number of K-shell vacancies and to the number of available quasifree target electrons, are plotted as a function of the adiabaticity parameter η (for the cross-section values, also compare Table I). The error bars shown in the figure account for both the statistical and systematic uncertainties of the individual measurements. The K-REC data which have been reported in the literature for high-Z systems ($Z \geq 54$), i.e., $Xe^{54+} \rightarrow$ Be at 197 MeV/u [19] and $Dy^{66+} \rightarrow$ Ar at 294 MeV/u [26], are given additionally.

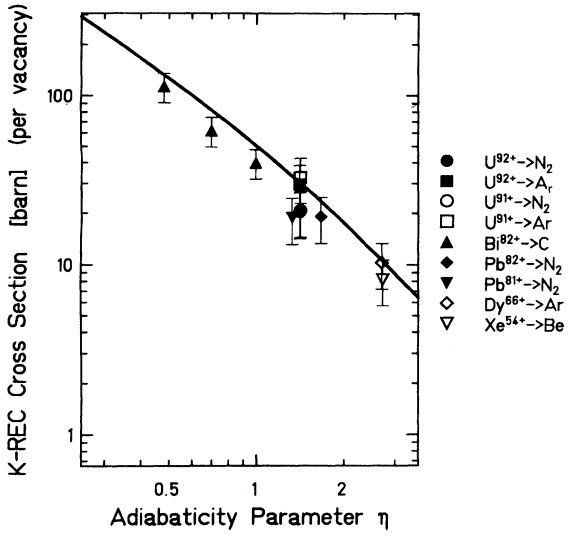

FIG. 10. Measured K-REC cross sections for $Z \geq 54$ normalized to the number of K-shell vacancies and to the number of target electrons in comparison with the dipole approximation (solid line). The Xe and Dy data are taken from Refs. [19] and [26], respectively.

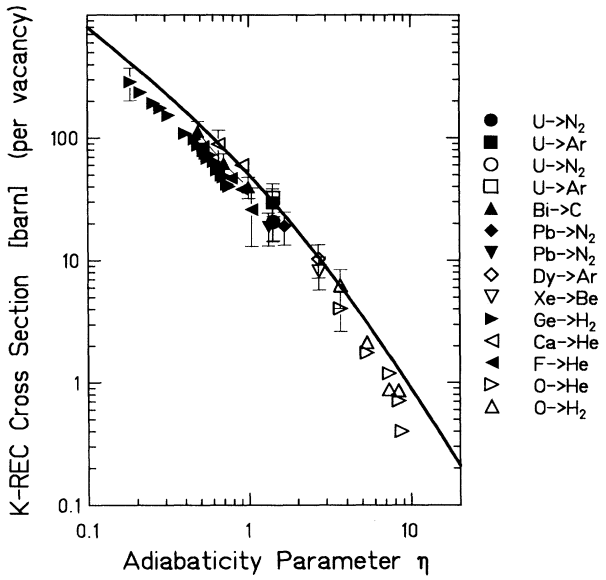

FIG. 11. Total K-REC cross sections normalized to the number of K-shell vacancies and to the number of target electrons plotted vs the adiabaticity parameter η [see Eq. (11)] for different collision systems: F→He [18], O→H_2, He [28], Ca→He [22], Ge→H_2 [25], Xe→Be [19], and Dy→Ar [26]. For the higher-Z data compare Table I. The solid line gives the prediction of the nonrelativistic dipole approximation.

The solid line in the figure presents the predictions of the nonrelativistic dipole approximation which was found almost to coincide with the relativistic exact calculation in the Z and η regimes of interest (compare Fig. 6 in Sec. III). The experimental data are reasonably well described by this simple theoretical model. Within the experimental uncertainties, the absolute values are also in general agreement with this approach.

Figure 11 comprises all the available K-REC data (for the low-Z data compare Refs. [18], [22], [25], and [28]). For each of the individual data sets we plot only one error bar describing the systematic uncertainties as estimated by the authors. Generally, the statistical errors are smaller than or comparable to the size of the data points. The bulk of data covers a Z regime of $8 \leq Z \leq 92$, with η values ranging from 0.1 up to about 10, and related kinetic beam energies between 1 and about 300 MeV/u. The results of the nonrelativistic scaling law are given in addition [see Eq. (2)] (compare the full line in Fig. 11). Comparing Figs. 10 and 11 one has to emphasize that a 20–30% overall deviation between experiment and theory, reported by Stöhlker *et al.* [25], Tribedi *et al* [27], and Vane *et al.* [28] as a common feature for the K-REC process seems to be slightly reduced if the high-Z data are considered. Nevertheless, Fig. 11 demonstrates that a systematic discrepancy between experiment and theory still remains. For high-Z systems the calculated relativistic angular distribution of REC was presumed in order to extract the proper total cross-section values. This procedure seems to be a crucial point in combining the experimentally observed differential values with total cross-section values for high-Z systems. For lighter-Z systems the ordinary dipole distribution was applied, as it provides sufficient accuracy.

V. TOTAL REC CROSS SECTIONS

In order to obtain additional information about radiative electron capture, in Fig. 12 we present all available data for total electron capture from light target atoms into bare, high-Z projectiles. The corresponding charge-changing cross sections plotted in the figure are normalized to the number of target electrons. The data were collected at the Lawrence Berkeley Laboratory's BEVALAC and at the FRS and ESR facilities (for the BEVALAC data compare [20] and [57]; for the FRS and ESR data, see Table I). The error bars given in the figure are due to the statistical as well as systematic uncertainties of the individual measurements. For this data presentation we applied the same η definition as given by Eq. (11). In Fig. 12 the presentation is restricted to the high-velocity regime, where electron pickup by the projectile from light target atoms is dominated by far by radiative capture. This feature is illustrated in Fig. 13, where the total electron-capture cross sections are plotted versus target atomic number Z_T for 295-MeV/u bare uranium ions. The measured data are compared with theoretical predictions for the two competing electron-capture processes, i.e., for REC and nonradiative electron capture (NRC). For NRC, the relativistic eikonal approximation was applied [58], which yields estimates for cross sections that are accurate within a factor of 2 [20,59]. For REC, the Stobbe theory [2] was used (Sec. II A). As seen in Fig. 13, a very good agreement between the predicted Z_T dependence of the cross sections and the experimental data is observed. In particular, these

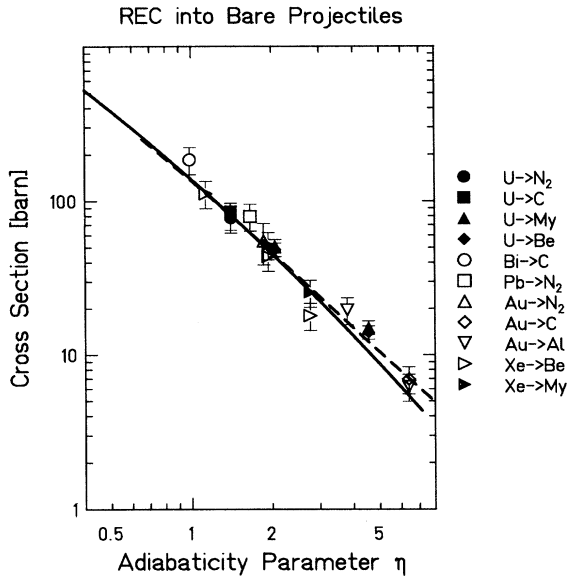

FIG. 12. Total electron-capture cross sections per target electron measured for heavy bare ions ($Z \geq 54$) in collisions with light target atoms (molecules). The results are plotted as a function of the η parameter and are compared with the result of a relativistic exact calculation for $Z = 80$ (dashed line) as well as with the prediction of the nonrelativistic dipole approximation (full line).

experimental data illustrate that for $Z_T \leq 13$ the NRC contribution to the total electron pickup can be neglected in the case of U^{92+} projectiles at 295 MeV/u. However, for the Ar target, NRC contributes considerably to the total capture cross section. The same observation has already been discussed for H-like uranium projectiles at the same collision energy [60]. Moreover, we have to note

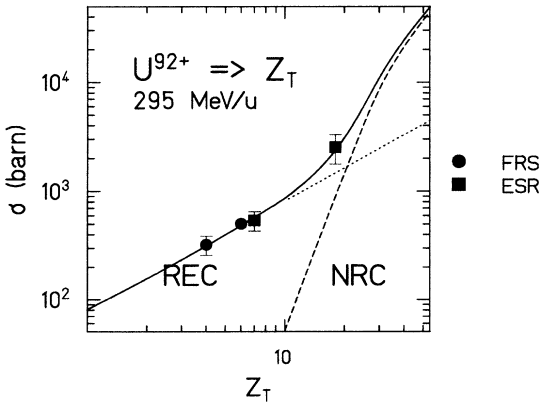

FIG. 13. Total electron-capture cross sections for bare U^{92+} at 295 MeV/u colliding with gaseous targets (see ■ for $U^{92+} \rightarrow N_2$, Ar) and with solid targets (see ● for $U^{92+} \rightarrow$ Be, C). For N_2 the cross section per atom is given. The results are compared with the theoretical cross-section predictions for the NRC and the REC processes (dashed and dotted lines). The resulting total electron-capture cross sections are given by the full line.

that the presentation of Fig. 12 includes data from solid targets with typical densities of 10^{23} particles/cm^3 as well as from gaseous targets with densities of about 10^{13} particles/cm^3. Therefore, Fig. 13 clearly demonstrates that target density effects do not influence the electron-capture probability for bare, high-Z ions at relativistic energies. This observation can be explained on the basis of the already discussed projectile n dependence of the REC process (Sec. III). It was shown that radiative capture predominantly occurs into the innermost bound projectile state. As a consequence, the K- and L-REC cross sections essentially determine the total cross-section values. Therefore, it would be of interest to study possible density effects by using few-electron, high-Z ions where the K and L shells are fully or partially blocked.

The data plotted in Fig. 12 are compared with theoretical cross-section values. The exact relativistic cross sections for various Z values diverge slightly at higher-η parameters (Fig. 7). Within the overall experimental accuracy the data are not sensitive on such a slight cross-section variation with atomic number Z, in particular for lower-η values. Therefore, only the relativistic exact results for $Z = 80$ are plotted in the figure. The calculation considers REC into the K, L, and M shells of the projectile. The $Z = 80$ value was applied, as it is close to the atomic number of the projectile systems used at the largest η values (compare Table I and Fig. 12). Additionally, the results of the nonrelativistic approach are shown by the full line. In general, excellent agreement between experiment and theory is found in Fig. 12. The experimental data are, within the error bars, not sensitive to the slight cross-section variation predicted by the relativistic theory for different Z systems at one common η parameter, especially for $\eta \leq 3$. At the higher-η regime, the results of the fully relativistic calculation performed for $Z = 80$ already deviate from the predictions of the nonrelativistic approach. In fact, the result of the latter approach seems to underestimate slightly the measured cross sections at high-η values.

VI. SUMMARY AND FUTURE ASPECTS

For fast collisions of bare high-Z projectiles with low-Z target atoms, radiative electron capture is the only relevant charge-changing process. In the present paper, we studied this process experimentally and theoretically for various high-Z projectiles up to uranium, with particular emphasis on K-shell capture. By measuring the x-rays emitted in coincidence with the down-charged ions, we were able to obtain almost background-free REC spectra. In this way, we measured and analyzed (1) angle-differential cross sections, (2) cross sections for K-REC, and (3) total REC cross sections for capture into all shells.

(1) Angle-differential cross sections, gained by a detailed analysis of the spectral line shapes, were compared with the results of fully relativistic calculations. The theoretically predicted pronounced deviations from a standard $\sin^2\theta$ distribution (suggested by the nonrelativistic dipole approximation) were found to be in good agreement with the experimental data. In fact, such an agree-

ment between experiment and theory has already been found in the more complicated case of subshell-resolved L-REC of He-like uranium at 89 MeV/u [54]. Very good agreement has also been obtained for the L- to K-REC differential cross-section ratio in $U^{92+} \rightarrow N_2$, Ar. In general, angle-differential REC cross sections are extremely sensitive to details of the atomic wave functions, and hence give a detailed insight into the atomic structure of high-Z projectile ions. Specifically, K-REC angular distributions are strongly influenced by magnetic transitions [8,51]. Because predictions of theoretical calculations have been confirmed in many examples, one may rely on this theory in cases in which total cross sections have been derived on the basis of the theoretical angular distribution by using experimental results obtained at only one observation angle. This point enters crucially into determination of all total cross sections discussed at length throughout the paper.

(2) By combining our results with published K-REC data, we obtain a systematics of cross sections covering almost the entire range of projectile charges. It is found that, in general, the experimental results are in a good overall agreement with a scaling law derived from the nonrelativistic dipole approximation. The various experimental data group closely together as a function of the adiabaticity parameter η, and follow a universal η scaling. There is still a slight discrepancy of approximately 20% between the data and results of the nonrelativistic dipole approximation. Although this approximation is not valid for high-Z projectiles, its results are close to those of exact relativistic calculations, an agreement that must be regarded as fortuitous.

(3) New data for REC into all projectile shells are combined with published data for $Z \geq 54$ and are presented in a systematic manner, similarly as for K-REC. As is the case for K-REC, the simple dipole approximation yields results that are very close to those of exact relativistic calculations including the K, L, and M shells. Also in this case there is an excellent agreement between experiment and theory for total cross sections. From these two findings one may conclude that it is appropriate, for practical purposes, to use the simple nonrelativistic approach for estimating total REC cross sections even for high-Z projectiles but not too high collision energies. This cross-section scaling is of interest, e.g., for furnishing a luminosity gauge in experiments dealing with light gaseous targets, as it yields simple but reliable cross-section estimates. For high beam energies ($E_{kin} > 500$ MeV/u) the application of the exact relativistic theory is certainly more appropriate. The remaining slight systematic discrepancy between theory and experiment is still an open question, which may be resolved by angle-differential measurements for low-Z as well as high-Z projectiles. It should be pointed out that the main contribution to total REC cross sections arises from K-REC. Therefore, if the projectile has an occupied K shell, one should not apply the nonrelativistic approach, since for higher shells the fortuitous agreement with exact results does not persist.

In the near future, one will be able to study the photon angular distribution of RR directly by means of electron target devices at storage rings. This technique will provide a direct comparison between shell-resolved RR and REC cross sections, which opens up the possibility of examining the influence of the target atom on the REC process. A detailed test of the validity range of the commonly applied impulse approximation is needed, if one wants to extract spectroscopic information about the projectile atomic structure from the REC spectra [26,55]. For the latter, recoil-ion momentum spectroscopy [61] provides a very sensitive tool, allowing one to measure the target recoil momentum (disregarded in the impulse approximation) in coincidence with the momentum of the REC photon as well as in coincidence with the down-charged ions.

Note added in proof. Relativistic calculations performed for photoionization cross sections by Ron *et al.* [65] confirm a remarkable agreement between nonrelativistic dipole and full relativistic multipole results. The phenomenon is explained in terms of an approximate cancellation among relativistic, retardation, and multipole effects which occurs only for s subshells.

ACKNOWLEDGMENTS

The support from the ERS group (K. Beckert, H. Eickhoff, B. Franzke, F. Nolden, P. Spädtke, and M. Steck) is gratefully acknowledged. We are also indebted to M. Jung, T. Kandler, O. Klepper, M. Kucharski, G. Münzenberg, and F. Nickel for the fruitful collaboration, and to W. E. Meyerhof for providing us with the charge-exchange data measured at the BEVALAC. The work of two of us (Z.S. and A.W.) was supported by GSI in Darmstadt and by the State Committee for Scientific Research (Poland) under research grant No. 201779101.

[1] J. R. Oppenheimer, Phys. Rev. **31**, 349 (1928).
[2] M. Stobbe, Ann. Phys. **7**, 661 (1930).
[3] R. J. Gould, Astrophys. J. **219**, 250 (1981).
[4] B. F. Rozsnyai and V. L. Jacobs, Astrophys. J. **327**, 485 (1988).
[5] L. Bracci, G. Fiorentini, and O. Pizurra, Phys. Lett. **85B**, 280 (1979).
[6] P. Baratella, G. Puddu, and P. Quarati, Z. Phys. A **300**, 263 (1981).
[7] G. Soff and J. Rafelski, Z. Phys. D **14**, 187 (1989).
[8] A. Ichihara, T. Shirai, and J. Eichler, Phys. Rev. A **49**, 1975 (1994).
[9] G. Raisbeck and F. Yiou, Phys. Rev. Lett. **4**, 1858 (1971).
[10] H. W. Schnopper, H. Betz, J. P. Devaille, K. Kalata, A. R. Sohval, K. W. Jones, and H. E. Wegner, Phys. Rev. Lett. **29**, 898 (1972).
[11] P. Kienle, M. Kleber, B. Povh, R. M. Diamond, F. S. Stephens, E. Grosse, M. R. Maier, and D. Proetel, Phys. Rev. Lett. **31**, 1099 (1973).
[12] M. Kleber and D. H. Jakubassa, Nucl. Phys. A **252**, 152 (1974).
[13] R. Shakeshaft and L. Spruch, Phys. Rev. Lett. **38**, 175

(1977).
[14] R. Schule, H. Schmidt-Böcking, and I. Tserruya, J. Phys. B **10**, 889 (1977).
[15] J. A. Tanis and S. M. Shafroth, Phys. Rev. Lett. **40**, 1174 (1978).
[16] E. Spindler, H.-D. Betz, and F. Bell, Phys. Rev. Lett. **42**, 832 (1979).
[17] J. A. Tanis, S. M. Shafroth, J. E. Willis, and J. R. Mowat, Phys. Rev. A **23**, 366 (1981).
[18] H. Tawara, P. Richard, and K. Kawatsura, Phys. Rev. A **26**, 154 (1982).
[19] R. Anholt, S. A. Andriamonje, E. Morenzoni, Ch. Stoller, J. D. Molitoris, W. E. Meyerhof, H. Dowman, J.-S. Xu, Z.-Z. Xu, J. O. Rasmussen, and D. H. H. Hoffmann, Phys. Rev. Lett. **53**, 234 (1984).
[20] W. E. Meyerhof, R. Anholt, J. Eichler, H. Gould, Ch. Munger, J. Alonso, P. Thieberger, and H. E. Wegner, Phys. Rev. A **32**, 3291 (1985).
[21] R. Anholt, Ch. Stoller, J. D. Molitoris, D. W. Spooner, E. Morenzoni, S. A. Andriamonje, W. E. Meyerhof, H. Dowman, J.-S. Xu, Z.-Z. Xu, J. O. Rasmussen, and D. H. H. Hoffmann, Phys. Rev. A **33**, 2270 (1986).
[22] J. A. Tanis, M. W. Clark, K. H. Berkner, E. M. Bernstein, W. G. Graham, R. J. McDonald, R. H. McFarland, J. R. Mowat, D. W. Mueller, A. S. Schlachter, J. W. Stearns, and M. P. Stöckli, J. Phys. **48**, 207 (1987). The cross sections for $Ca^{19+} \rightarrow He$ and for $Ca^{20+} \rightarrow He$ have been reduced by 20% to correct for a systematic error discovered after publication [28].
[23] K. I. Hino and T. Watanabe, Phys. Rev. A **36**, 581 (1987).
[24] K. I. Hino and T. Watanabe, Phys. Rev. A **39**, 3373 (1989).
[25] Th. Stöhlker, C. Kozhuharov, A. E. Livingston, P. H. Mokler, Z. Stachura, and A. Warczak, Z. Phys. D **23**, 121 (1992).
[26] H. F. Beyer, K. D. Finlayson, D. Liesen, P. Indelicato, C. T. Chantler, R. D. Deslattes, J. Schweppe, F. Bosch, M. Jung, O. Klepper, W. König, R. Moshammer, K. Beckert, H. Eickhoff, B. Franzke, A. Gruber, F. Nolden, P. Spätke, and M. Steck, J. Phys. B **26**, 1557 (1993).
[27] L. C. Tribedi, V. Nanal, M. R. Press, M. B. Kurup, K. G. Prasad, and P. N. Tandon, Phys. Rev. A **49**, 374 (1994).
[28] C. R. Vane, S. Datz, P. F. Dittner, J. Giese, N. L. Jones, H. F. Krause, T. M. Roessel, and P. S. Peterson, Phys. Rev. A **49**, 1847 (1994).
[29] M. Pajek and R. Schuch, Phys. Rev. A **46**, 6962 (1992).
[30] P. H. Mokler, in *The Physics of Highly Charged Ions,* AIP Conf. Proc. No. 274, edited by P. Richard, M. Stöckli, C. L. Cocke, and C. D. Lin, (AIP, New York, 1993), p. 515.
[31] A. Müller, Nucl. Instrum. Methods Phys. Res. B **87**, 34 (1994).
[32] R. W. Schmieder, in *Proceedings of the NATO Workshop on the Physics of Highly Ionized Atoms, Cargese, Corsica June 1988,* edited by R. Marrus (Plenum, New York, 1990), p. 231.
[33] J. P. Briand, P. Chevallier, P. Indelicato, K. P. Ziock, and D. D. Dietrich, Phys. Rev. Lett. **65**, 2761 (1990).
[34] Th. Stöhlker, P. H. Mokler, H. Geissel, R. Moshammer, P. Rymuza, E. M. Berstein, C. L. Cocke, C. Kozhuharov, G. Münzenberg, F. Nickel, C. Scheidenberger, Z. Stachura, J. Ullrich, and A. Warczak, Phys. Lett. A **168**, 285 (1992).
[35] H. F. Beyer, D. Liesen, F. Bosch, K. D. Finlayson, M. Jung, O. Klepper, R. Moshammer, K. Beckert, H. Eickhoff, B. Franzke, F. Nolden, P. Spädtke, and M. Steck, Phys. Lett. A **184**, 435 (1994).
[36] Th. Stöhlker, P. H. Mokler, K. Beckert, F. Bosch, H. Eickhoff, B. Franzke, M. Jung, T. Kandler, O. Klepper, C. Kozhuharov, R. Moshammer, F. Nolden, H. Reich, P. Rymuza, P. Spädtke, and M. Steck, Phys. Rev. Lett. **71**, 2184 (1993).
[37] R. Anholt, W. E. Meyerhof, X.-Y. Xu, H. Gould, B. Feinberg, R. J. McDonald, H. E. Wegner, and P. Thieberger, Phys. Rev A **36**, 1586 (1987).
[38] Th. Stöhlker, H. Geissel, H. Folger, C. Kozhuharov, P. H. Mokler, G. Münzenberg, D. Schardt, Th. Schwab, H. Stelzer, and K. Sümmerer, Nucl. Instr. Methods **61**, 408 (1991).
[39] R. E. Marrs, Comments. At. Mol. Phys. **27**, 57 (1991).
[40] F. Bosch, in *The Physics of Electronic and Atomic Collisions,* edited by T. Andersen, B. Fastrup, F. Folkmann, H. Knudsen, and N. Andersen, AIP Conf. Proc. No. 295 (AIP, New York, 1993), p. 3.
[41] C. Scheidenberger, H. Geissel, Th. Stöhlker, T. Brohm, A. Heinz, H. Irnich, M. de Jong, A. Magel, F. Nickel, M. Pfützner, K.-H. Schmidt, W. Schwab, S. Steinäuser, K. Sümmerer, B. Voss, and G. Münzenberg, GSI Scientific Report No. 93-1 (unpublished).
[42] K. Blasche, SIS Beam Development 1989-1991 GSI-Report No. GSI-SIS-INT/86-2 (unpublished).
[43] H. Geissel, P. Armbruster, K.-H. Behr, B. Blank, A. Brünle, H. G. Burkhard, K. H. Burkhard, G.-G. Clerc, M. Chen, J. P. Dufour, B. Franczak, Y. Fujita, J. J. Gaimard, E. Hanelt, R. Kirchner, O. Klepper, B. Langenbeck, F. Nickel, K. Poppensieker, M. D. Pravikoff, E. Roeckel, D. Schardt, K.-H. Schmidt, Th. Schwab, H. J. Schött, B. Sherrill, K. Sümmerer, H. Wollnik, G. Münzenberg, Nucl. Instrum. Meth. Phys. Res. B **70**, 286 (1992).
[44] B. Franzke, in *Application of Accelerators in Research and Industry '86,* edited by J. L. Duggan and I. L. Morgan (North-Holland, Amsterdam, 1987), p. 18.
[45] M. Jung, F. Bosch, K. Beckert, H. Eickhoff, B. Franzke, A. Gruber, P. Kienle, O. Klepper, W. Koenig, C. Kozhuharov, R. Mann, R. Moshammer, F. Nolden, U. Schaaf, G. Soff, P. Spädtke, M. Steck, Th. Stöhlker, and K. Sümmerer, Phys. Rev. Lett. **69**, 2164 (1992).
[46] C. Scheidenberger, H. Geissel, Th. Stöhlker, H. Folger, H. Irnich, C. Kozhuharov, A. Magel, P. H. Mokler, R. Moshammer, G. Münzenberg, F. Nickel, M. Pfützner, P. Rymuza, W. Schwab, J. Ullrich, and B. Voss, Nucl. Instrum. and Methods B **90**, 36 (1994).
[47] C. Scheidenberger, H. Geissel, H. H. Mikkelsen, F. Nickel, T. Brohm, H. Folger, H. Irnich, A. Magel, M. F. Mohar, G. Münzenberg, M. Pfützner, E. Roeckel, I. Schall, D. Schardt, K.-H. Schmidt, W. Schwab, M. Steiner, Th. Stöhlker, K. Sümmerer, D. J. Vieira, B. Voss, and M. Weber, Phys. Rev. Lett. **73**, 50 (1994).
[48] A. Burgess, Mem. Roy. Ast. Soc. **69**, 1 (1964).
[49] D. J. McLaughlin and Y. Hahn, Phys. Rev. A **43**, 1313 (1991).
[50] H. A. Bethe and E. E. Salpeter, *Quantum Mechanics of One- and Two-Electron Atoms* (Springer-Verlag, Berlin, 1957).
[51] J. Eichler, Phys. Rep. **193**, 165 (1990).
[52] S. Hultberg, B. Nagel, and P. Ollson, Ark. Fys. **38**, 8 (1967).
[53] J. H. Scofield, Phys. Rev. A **40**, 3054 (1989).

[54] Th. Stöhlker, H. Geissel, H. Irnich, T. Kandler, C. Kozhuharov, P. H. Mokler, G. Münzenberg, F. Nickel, C. Scheidenberger, T. Suzuki, M. Kucharski, A. Warczak, P. Rymuza, Z. Stachura, A. Kriessbach, D. Dauvergne, B. Dunford, J. Eichler, A. Ichihara, and T. Shirai, Phys. Rev. Lett. **73**, 3520 (1994).

[55] P. H. Mokler, Th. Stöhlker, C. Kozhuharov, Z. Stachura, and A. Warczak, Z. Phys. D **21**, 197 (1991).

[56] F. Biggs, L. B. Mendelsohn, and J. B. Mann, At. Data Nucl. Data Tables **16**, 201 (1975).

[57] W. E. Meyerhof (private communication).

[58] J. Eichler, Phys. Rev. A **312**, 112 (1985).

[59] A. Ichihara, T. Shirai, and J. Eichler, At. Data Nucl. Data Tables **55**, 63 (1993).

[60] Th. Stöhlker, P. H. Mokler, T. Kandler, C. Kozhuharov, R. Moshammer, P. Rymuza, Z. Stachura, A. Warczak, K. Beckert, F. Bosch, H. Eickhoff, B. Franzke, M. Jung, O. Klepper, F. Nolden, H. Reich, P. Spädtke, and M. Steck, *Abstracts of Contributed Papers, XVIII International Conference on the Physics of Electronic and Atomic Collisions, Aarhus 1993,* edited by T. Andersen, B. Fastrup, F. Folkmann, and H. Knudsen (Aarhus Universitet, Aarhus, 1993), p. 617.

[61] J. Ullrich, R. Dörner, S. Lencinas, O. Jagutzki, H. Schmidt-Böcking, and U. Buck, Nucl. Instrum. Methods Phys. Res. B **61**, 415 (1991).

[62] K. D. Finlayson, GSI-Report No. GSI-92-18 ISSN 0171-546 (unpublished).

[63] Th. Stöhlker, P. H. Mokler, K. Beckert, F. Bosch, H. Eickhoff, B. Franzke, H. Geissel, M. Jung, T. Kandler, O. Klepper, C. Kozhuharov, R. Moshammer, F. Nickel, F. Nolden, H. Reich, P. Rymuza, C. Scheidenberger, P. Spädtke, Z. Stachura, M. Steck, and A. Warczak, Nucl. Instrum. Methods B **87**, 64 (1994).

[64] Th. Stöhlker, P. H. Mokler, H. Geissel, E. M. Bernstein, C. L. Cocke, C. Kozhuharov, R. Moshammer, G. Münzenberg, F. Nickel, P. Rymuza, C. Scheidenberger, Z. Stachura, J. Ullrich, and A. Warczak, Rad. Eff. Def. Solids **126**, 319 (1993).

[65] A. Ron, I. B. Goldberg, J. Stein, S. T. Manson, R. H. Pratt, and R. Y. Yin, Phys. Rev. A **50**, 1312 (1994).